Computers in Biology and Medicine 187 (2025) 109794

Contents lists available at ScienceDirect

Computers in Biology and Medicine

journal homepage: www.elsevier.com/locate/compbiomed

Patient-specific lattice-Boltzmann simulations with inflow conditions from magnetic resonance velocimetry measurements for analyzing cerebral aneurysms

Mario Rüttgers [a,*], Moritz Waldmann [b], Shota Ito [c], Carolin Wüstenhagen [d], Sven Grundmann [d], Martin Brede [d], Andreas Lintermann [a]

[a] Jülich Supercomputing Centre (JSC), Forschungszentrum Jülich GmbH, Germany
[b] Institute of Aerodynamics and Chair of Fluid Mechanics (AIA), RWTH Aachen University, Germany
[c] Lattice Boltzmann Research Group, Institute for Mechanical Process Engineering and Mechanics, Karlsruhe Institute of Technology (KIT), Germany
[d] Institute of Fluid Mechanics, University of Rostock, Germany

ARTICLE INFO

Keywords:
Computational fluid dynamics
Hemodynamic flow
Non-Newtonian simulations
Carreau–Yasuda model

ABSTRACT

Magnetic resonance velocimetry (MRV) measurements were used as inflow conditions for lattice-Boltzmann (LB) simulations to analyze cerebral aneurysms. Unlike previous studies on larger vascular structures, aneurysm analysis involves smaller scales and higher pressure differences, making near-wall velocity measurements challenging with standard 3 Tesla scanners. To address this, the aneurysm geometry was scaled 5-fold for sufficient magnetic resonance velocimetry (MRV) resolution, with inflow measurements interpolated onto the simulation grid while ensuring dimensionless equivalence via the Reynolds number. Zero-velocity points were included near walls to enforce the no-slip condition if measurement points exceed the simulation domain. The proposed interpolation-based inflow method was compared to a nearest-neighbor approach and a parabolic velocity profile. It achieved the best agreement with MRV centerline velocity measurements (mean error: 3.12%), followed by the nearest-neighbor method (3.18%) and the parabolic profile (9.85%). The parabolic inflow led to centerline velocity overpredictions and total pressure underpredictions, while the nearest-neighbor approach underestimated the wall shear stress (WSS) and exhibited inconsistencies in wall normal stress (e.g., maximum WSS was 18.3% lower than with interpolation). Using the interpolated inflow method, Newtonian and non-Newtonian flows based on the Carreau–Yasuda model were compared. The non-Newtonian model showed lower centerline velocities and total pressure but higher WSS than the Newtonian case. These findings highlight the importance of accurate, patient-specific inflow conditions and the necessity of non-Newtonian modeling for reliable WSS predictions. Combining MRV measurements with non-Newtonian LB simulations provides a robust framework for personalized cerebral aneurysm hemodynamic evaluation.

1. Introduction

Aneurysms are dangerous vascular diseases that can be fatal if left untreated. They are characterized by the formation of arterial bulges, often developing in vessels with complex geometries, such as vascular bifurcations or tapering regions. These locations experience particularly high WSS and WSS gradients due to small curvature radii [1]. The disease results from degenerative changes in the vessel wall, and its progression is largely influenced by forces exerted by blood flow, which can ultimately lead to rupture.

According to [2], aneurysm rupture risk can be classified based on four key characteristics: (1) the flow type, determined by the direction of the incoming blood jet impinging on the vessel wall, (2) the aneurysm's size, (3) the location of the impact area, and (4) the size of the impact area. Since forces acting on the vessel wall play a crucial role in aneurysm formation, incorporating additional features related to WSS and WNS loads is highly desirable.

Currently, three primary approaches are used to supplement conventional analyses of cerebral aneurysms: (1) experimental analyses, sometimes validated using computational fluid dynamics (CFD) simulations, (2) purely numerical studies, and (3) hybrid approaches that combine experimental and numerical techniques.

Experimental investigations of aneurysm hemodynamics are often conducted using simplified models and blood-replacement fluids [3–5]. However, this approach makes it difficult to distinguish between errors

* Corresponding author.
E-mail address: m.ruettgers@fz-juelich.de (M. Rüttgers).

https://doi.org/10.1016/j.compbiomed.2025.109794
Received 27 September 2024; Received in revised form 30 January 2025; Accepted 1 February 2025
Available online 11 February 2025

caused by geometric simplifications and those resulting from the use of non-physiological fluid models. In [6], a patient-specific aneurysm model with an implanted flow diverter was analyzed using both MRV and CFD simulations. Although the study showed good agreement between numerical and experimental data, limitations were observed. The model was not scaled, leading to limited spatial resolution, and a Newtonian fluid was used, despite blood being non-Newtonian. As a result, significant deviations were found, particularly in the maximum velocity, which was 14.86% higher in the CFD simulation compared to the MRV measurement inside the flow diverter region.

Accurate fluid mechanics investigations of vascular systems require blood substitute fluids with properties closely matching those of human blood. This requires at least a correct representation of blood's nonlinear flow behavior. In [7], a CFD-based study quantified the relevance of this adaptation, revealing deviations of up to 63% in velocity magnitude between Newtonian and non-Newtonian fluid models at specific control points. However, direct experimental measurements with human blood are challenging due to coagulation and the associated changes in flow properties. Furthermore, MRV-based analyses of aneurysm models at real scale suffer from low spatial resolution, making model scaling desirable. However, scaling combined with Newtonian water–glycerin mixtures introduces deviations in the flow curve at low shear rates, leading to errors in recirculation and stagnation zones [8].

Better agreement with the real flow can be achieved using non-Newtonian fluids in 1:1 models. In [9], non-Newtonian model fluids produced larger recirculation areas compared to Newtonian fluids. The study in [10] used a full-scale patient-specific model with a polyacrylamide/glycerin fluid that approximates blood properties. Laser Doppler anemometry (LDA) measurements were performed to evaluate the effects of a flow diverter. Similarly, in [11], CFD calculations were successfully validated in an elastic aneurysm model using LDA measurements with a polyacrylamide-based fluid closely matching blood's non-Newtonian properties. However, unlike MRV, LDA cannot be performed in vivo, making it difficult to integrate into patient-specific workflows. Additional options for creating blood-analogous fluids for 1:1 models are discussed in [12,13].

Current medical imaging techniques lack the spatial resolution required to capture detailed patient-specific flow fields in vivo. This limitation prevents reliable fluid mechanics analyses, such as determining the WSS distribution on vessel walls, leading to an incomplete understanding of aneurysm formation, triggers, and disease progression. As a result, patient-specific prognoses regarding aneurysm development and implant effectiveness remain uncertain.

The second major approach to aneurysm analysis relies on purely numerical CFD simulations. These are frequently used to study flow characteristics and identify predictive rupture risk parameters, such as vortex strength. Many of these simulations use simplified, generic geometries, such as the symmetric semicircular model in [14]. More advanced studies analyze real patient-specific vessel geometries. For instance, in [15], CFD simulations of aneurysm models from 12 patients were used to predict rupture risk based on regions of exposed low WSS. Similarly, the study in [16] combined CFD simulations with morphological analysis of internal carotid artery geometries from 52 patients with intracranial aneurysms. A functional principal component analysis of geometric and fluid dynamic features revealed correlations between aneurysm location, rupture status, and hemodynamic factors, aiding in patient clustering for rupture risk assessment.

The Multiple Aneurysms AnaTomy Challenge (MATCH) summarizes the results of many working groups regarding the influence of vessel morphology on hemodynamics [17]. In these results, the focus is not only on the representation of the pulsatile flow in the patient-specific simulation domain, but also on the evaluation of the WSS in the aneurysm and the evaluation of implants [18] and their influence on the vessel geometry [19].

While the previously mentioned numerical studies assume Newtonian fluids, considering blood's non-Newtonian properties provides additional insights. Studies such as [20–22] investigated how non-Newtonian properties affect WSS, concluding that while general flow patterns remain similar, recirculation zones differ. Furthermore, Newtonian models systematically underestimate WSS, which can impact rupture risk assessment. Other studies found significant differences in flow topology between Newtonian and non-Newtonian fluids [7]. In [23,24], a non-Newtonian LB model based on the Carreau–Yasuda (CY) equation with single Bhatnagar–Gross–Krook (BGK) and multiple relaxation time collision operators was used to assess WSS distributions. They found that non-Newtonian fluids exhibit more oscillatory WSS and greater fluctuations at high Reynolds numbers.

Although numerical methods show strong potential for analyzing hemodynamics, simulation accuracy is highly dependent on boundary conditions. Small deviations in the geometry, e.g., due to imaging resolution limitations or uncertainties in inflow/outflow conditions, can lead to incorrect results. Consequently, key flow characteristics, such as vortex structures and flow separation, are often misrepresented, potentially leading to fluid mechanics and clinical misinterpretations.

Hybrid approaches that integrate experimental and numerical methods have recently gained attention. Studies such as [25,26] incorporated 4D-flow magnetic resonance imaging (MRI) data as inflow conditions for CFD simulations of aortic flow, demonstrating the importance of accurate boundary conditions for capturing complex flow regimes. Similarly, [27] developed a non-invasive methodology for determining the 3D flow environment of the dural venous sinuses. They combined CFD with phase-contrast magnetic resonance venography, achieving pressure gradient errors of only 5% compared to venous manometry.

Applying such hybrid methods to cerebral aneurysms is more challenging due to their smaller spatial scale and higher pressure differences, making velocity measurements with standard 3 Tesla scanners difficult, especially near vessel walls. This study advances hybrid approaches by scaling aneurysm geometries 5-fold to achieve sufficient MRV resolution. The measured inflow conditions are then rescaled and interpolated onto CFD simulation grids. All flow variables exhibit dimensionless equivalence when scaled or re-scaled according to the Reynolds number. Measurements close to walls can lie outside the simulation domain, caused by funnel-shaped connections between the aneurysm model and hoses of the measuring devices. Therefore, if measurements points exceed the simulation domain, interpolation is done with zero-velocity points to satisfy the no-slip condition. The CFD simulations are conducted with an LB solver, whose potential for simulating non-Newtonian flows with the CY model has been underlined in the studies mentioned before.

The new method aims to combine the strengths of experimental and numerical approaches while mitigating their weaknesses. The measurement data of the original flow provide the correct and patient-specific inflow topology, while the simulation contributes to the accessibility of highly resolved flow data and the resilience of derivable quantities. These quantities would be less accurate even when measured with the scaled geometry (e.g. near-wall velocities or WSS), or impossible to be measured (e.g. the 3D pressure field). The weaknesses of the individual methods are eliminated: too low resolution of the measurement data and the risk that simulations develop incorrect flow topologies due to inaccurate inflow conditions. The following questions are examined for a reconstructed geometry from a patient suffering from a cerebral aneurysm:

1. What grid resolution is required for the MRV-LB-based simulations?
2. Can simulations reproduce centerline velocities from MRV measurements?
3. How does the proposed inflow condition compare to simpler alternatives?

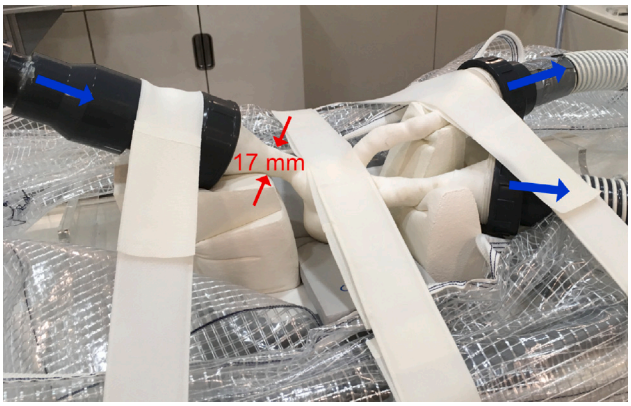

Fig. 1. 3D aneurysm model for the MRV measurements.

4. Is simulating non-Newtonian flow necessary? (The MRV measurements and comparisons for 1.–3. are for a Newtonian fluid)

The investigation builds the foundation for developing digital twins for a patient's personalized evaluation of the rupture risk or implant design, e.g., the design of flow diverters or stents.

The manuscript is structured as follows. Section 2 explains the methods of the hybrid MRV-LB approach. The results are presented in Section 3, followed by a summary and discussion in Section 4, and a conclusion in Section 5.

2. Methods

This section provides an overview over the measurement and computational methods. Section 2.1 details the MRV measurement techniques. Section 2.2 provides information on the numerical methods for generating the computational meshes and conducting simulations, the computational domain, the boundary conditions, and the model used for simulating a non-Newtonian fluid behavior.

2.1. Magnetic resonance velocimetry

MRV is a flow measurement technique that has been successfully developed in recent years for the use on humans. For a detailed description of the principles of the technique, the reader is referred to [28].

The MRV measurement of the aneurysm model in the current study is performed on the medical MRI scanner Magnetom Tim TRIO (Siemens, Erlangen, Germany) with a magnetic field of 3 Tesla. This MRI scanner is particularly suitable for flow measurements as it generates an extremely homogeneous magnetic field.

The aneurysm model for the MRV measurements was extracted from computed tomography (CT) data. It is equipped with transition parts and threads so that the inlets and outlets of the aneurysm can be connected to hoses. The model is then manufactured from polyamide using the laser sintering process, as the model cannot consist of any magnetic or metallic parts inside of the field of view. To ensure a sufficient resolution in the MRV measurement, the aneurysm is scaled 5-fold.

Scaling flow geometries is a widely used approach in fluid mechanics to enhance experimental resolution, accessibility, and feasibility. This technique is based on the Reynolds number, a dimensionless quantity representing the ratio of inertial forces to viscous forces in a flow. The Reynolds number is derived through the non-dimensionalization of the governing equations. To achieve dynamic similarity between in-vitro experiments and in-vivo conditions, the fluid viscosity and flow rate were adjusted to match the Reynolds number corresponding to arterial flow entering the aneurysm. All flow variables, including WSS and its gradients, exhibit dimensionless equivalence when scaled according to the Reynolds number.

Table 1
MRV measurement parameters.

Parameter name	Parameter value
Field of view	$384 \times 288 \times 120$ mm^3
Isotropic resolution	1 mm
Echo time	3.1 ms
Repetition time	5.9 ms
Flip angle	35°
Velocity encoding	0.7 m/s (isotropic)
Acquisition time	82 min

The experimental setup consists of a 300 L tank filled with a water–glycerin mixture. 1 g/l copper sulfate is added to perform as a contrast agent. An axial 2.2 kW pump (Matrix 5, EBARA Pumps Europe S.p.A., Italy) transports the fluid through hoses to the aneurysm model. Fig. 1 shows the 3D model that has been used for the measurements with a diameter of $d_{MRV} = 0.017$ m. After pumping the flow through the system for approximately half an hour, the temperature of the fluid settled at 22.7 °C. The boundary conditions observed with suitable sensors were a flow rate of 6.55 l/min leading to an inlet bulk velocity of $\bar{U}_{inl} = 0.48$ m/s, a kinematic viscosity of the water–glycerin mixture of $\nu = 1.16 \cdot 10^{-5}$ m^2/s, and a density of $\rho = 1170$ kg/m^3.

The measurements were performed using a custom velocity-sensitive gradient echo sequence. The parameters used can be seen in Table 1. It is important to note that the sequence settings are highly dependent on the specific MRI scanner being used. These settings may vary based on the scanner's hardware and should be individually optimized for each MRI system to achieve the highest possible flow measurement precision. Table 1 provides the settings used in this study for completeness and experimental reproducibility.

2.2. Numerical methods

Unstructured hierarchical Cartesian meshes are generated with the massively parallel mesh generator of the multi-physics, open-source simulation framework m-AIA [29],[1] which is an extended version of the formerly known Zonal Flow Solver (ZFS) [30]. The meshes are based on an octree structure implied by the iterative subdivision of an initial cube surrounding the region of interest (ROI), i.e., the aneurysm [31]. Starting from the initial cube, cubes are decomposed into eight sub-cubes for a pre-defined number of refinement steps. The parent–child relations of cubes and sub-cubes constitute the octree structure of the mesh. Cells that are located outside the ROI are deleted. At each refinement step, the domain is decomposed by a Hilbert decompositioning method using space filling curves as described in [32]. The resulting mesh is stored by efficient parallel I/O routines using the Network Common Data Form (NetCDF) format [33].

The governing equations of the LB method for conducting the CFD simulations are based on the BGK model approximation [34]

$$\frac{\partial \boldsymbol{f}}{\partial t} + \boldsymbol{\xi} \cdot \boldsymbol{f} = -\omega(\boldsymbol{f} - \boldsymbol{f}^{eq}), \tag{1}$$

$$\boldsymbol{f}^{neq} = \boldsymbol{f} - \boldsymbol{f}^{eq}, \tag{2}$$

with the particle probability distribution functions (PPDFs) $\boldsymbol{f} = \boldsymbol{f}(\boldsymbol{x}, \boldsymbol{\xi}, t)$, time t, location $\boldsymbol{x}$, microscopic velocity $\boldsymbol{\xi}$, collision frequency ω, and Boltzmann–Maxwellian distribution function $\boldsymbol{f}^{eq}$. In [34], Eq. (1) is discretized for a small time increment δt yielding

$$\boldsymbol{f}_i(\boldsymbol{x} + \boldsymbol{\xi}_i \delta t, \boldsymbol{\xi}, t + \delta t) - \boldsymbol{f}_i(\boldsymbol{x}, \boldsymbol{\xi}_i, t) = - \omega(\boldsymbol{f}_i(\boldsymbol{x}, \boldsymbol{\xi}_i, t) - \boldsymbol{f}_i^{eq}(\boldsymbol{x}, \boldsymbol{\xi}_i, t)). \tag{3}$$

[1] m-AIA https://git.rwth-aachen.de/aia/m-AIA/m-AIA.

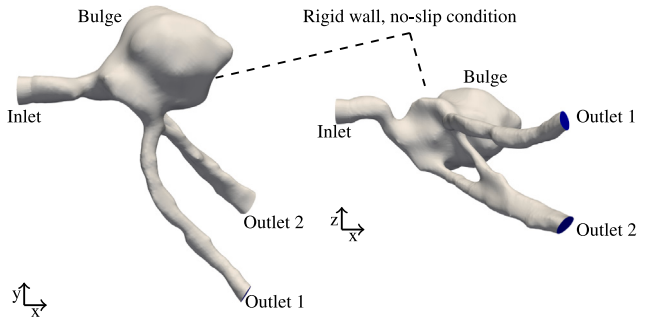

Fig. 2. Computational domain and the corresponding coordinate system.

The discretization is based on the D3Q27 model [35], with $i \in \{1, 2, 3, \ldots, Q\}$ directions. The discrete Boltzmann–Maxwellian distribution function reads

$$f_i^{eq} = wc_i\rho\left(1 + \frac{\boldsymbol{\xi_i}\cdot\boldsymbol{u}}{c_s^2} + \frac{1}{2}\left(\frac{\boldsymbol{\xi_i}\cdot\boldsymbol{u}}{c_s^2}\right)^2 - \frac{\boldsymbol{u}\cdot\boldsymbol{u}}{2c_s^2}\right), \tag{4}$$

with the isothermal speed of sound $c_s = 1/\sqrt{3}$, density ρ, fluid velocity vector $\boldsymbol{u} = (u, v, w)^T$, and weight coefficients wc_i [35].

The macroscopic variables ρ and $\boldsymbol{u}$ can be computed by

$$\rho = \sum_{i=1}^{Q} f_i, \tag{5}$$

$$\rho\boldsymbol{u} = \sum_{i=1}^{Q} \boldsymbol{\xi}_i \cdot f_i. \tag{6}$$

The static pressure p_s is obtained from the density by $p_s = c_s^2\rho$. Note that p_{tot} is the total pressure, expressed as the sum of p_s and the dynamic pressure $p_d = \rho|\boldsymbol{u}|^2/2$, where $|\boldsymbol{u}|$ is the velocity magnitude.

The computational domain and its coordinate system are illustrated in Fig. 2. It is scaled by a factor of 1:5 compared to the 3D model used for the MRV measurements. To assure a smooth connection to the MRV devices, the vessels of the 3D model shown in Fig. 1 are widened near the inlet and the outlets. Therefore, the inlet of the computational domain begins at the end of the conical inflow region. For simulations with Newtonian fluids, the Reynolds number is set to $Re = \bar{U}_{inl}\, d/\nu = 703$, where $\bar{U}_{inl} = 0.48$ m/s matches with the experimental data, and $d_{CFD} = 0.0034$ m is the diameter at the inlet of the computational domain. The kinematic viscosity is adapted to account for the differences in d_{MRV} and d_{CFD} while matching the Reynolds number of the MRV measurements.

An interpolated bounce-back scheme is used to satisfy the no-slip condition at the inner walls of the vessel [36]. That is, an interpolated distribution is reflected at the intersection between the grid and the 3D model. If the wall is located exactly halfway between the outer and inner cell centers, this condition reduces to simple halfway bounce-back. Furthermore, a rigid wall without fluid–structure interaction is assumed. At the two outlets, a constant pressure is prescribed and the velocity is extrapolated from the inner cells.

The following three different types of inflow conditions are investigated:

1. **Interpolation-based inflow condition**
   In this approach, velocity values at simulation mesh points are computed using interpolation. A Cartesian stencil with eight interpolation points is constructed to ensure a balanced representation of the surrounding flow structure. These points are evenly distributed in space around the mesh point to form a local Cartesian coordinate system. For each octant of this system, the nearest MRV measurement point is selected. If no valid measurement point exists in an octant, it is assumed that the octant is intersected by the geometry. In such cases, the minimum distance to the boundary wall is determined, and a zero-velocity interpolation point is placed at the boundary. The final velocity at each mesh point is computed using inverse distance interpolation from the surrounding interpolation points.
2. **Nearest-neighbor inflow condition**
   This method directly assigns velocity values from the MRV measurements using a nearest-neighbor algorithm. Since MRV data provide voxel-centered velocity distributions, i.e., each velocity vector represents the average velocity within a voxel, the velocity of a computational mesh point is taken from the voxel in which it resides. This approach is straightforward to implement, making it a practical alternative to the more complex interpolation-based method. However, its accuracy is limited by the spatial resolution of the MRV data, particularly near the boundaries, as discussed in Section 1.
3. **Parabolic inflow condition**
   The third inflow condition assumes a parabolic velocity profile for three-dimensional pipe flow, with a maximum inlet velocity in the x-direction given by $U_{inl}^{max} = 2\bar{U}_{inl}$. Like the nearest-neighbor method, this approach is simple to implement, making it a viable option if it does not compromise simulation accuracy.

For the non-Newtonian simulations, two models are integrated into the LB solver. The simpler model of the two is the power-law model [37]

$$\mu = \lambda\dot{\gamma}^{n-1}, \tag{7}$$

with the dynamic viscosity μ, shear rate $\dot{\gamma}$, consistency index λ, and non-dimensional power-law exponent index n. The indices λ and n are empirical curve-fitting parameters. With this model, two types of non-Newtonian fluids can be described: for $n < 1$, fluids of a shear-thinning type are obtained, while for $n > 1$, shear-thickening flow is modeled. In the case of $n = 1$, a Newtonian behavior of the viscosity is recovered.

The power-law model applies only to a restricted range of shear rates. It is unable to predict zero- or infinite-shear viscosities, yielding strongly fluctuating local viscosities [38]. This problem is pertinent, especially for the simulation of non-Newtonian flow using the LB method, since stability problems arise for approaching zero-viscosity values.

The second model that is implemented in the LB solver is an alternative to the power-law model which considers zero- and infinity-viscosity values, i.e., the CY model based on the viscosity equation from [39]

$$\frac{\mu - \mu_\infty}{\mu_0 - \mu_\infty} = [1 + (\lambda\dot{\gamma})^a]^{(n-1)/a}. \tag{8}$$

The additional parameters of the CY model are the zero viscosity μ_0, and infinite viscosity μ_∞. They guarantee constant viscosity as the shear rate tends to either zero or infinity, while a describes the transition between the Newtonian plateau and power law region. The CY model is used for the non-Newtonian LB simulations in this study, with $\mu_\infty = 0.0035$ Pa s, $\mu_0 = 0.056$ Pa s, $\lambda = 1656.6$ s, $n = 0.3568$, and $a = 2.0$ [40].

The WSS (σ^{WSS}), which is analyzed in Section 3, is computed based on the rate-of-strain tensor $\epsilon = \frac{1}{2}(\nabla\boldsymbol{u} + \nabla\boldsymbol{u}^T)$, and stress tensor $\sigma = 2\mu\epsilon + p_s I$, where I is the identity matrix. It is defined as the magnitude of the tangential component of the surface traction

$$t^* = \sigma \cdot n^*, \tag{9}$$

$$\tau = t^* - (t^* \cdot n^*)n^*, \tag{10}$$

$$\sigma^{WSS} = \|\tau\|, \tag{11}$$

where n^* is the outward unit normal to the boundary of the domain, t^* the surface traction, and τ its tangential component.

The WNS (σ^{WNS}) is the normalized total pressure acting on the boundary in the wall-normal direction

$$\sigma^{WNS} = \frac{p_{tot}}{\bar{p}_{tot}^{inl}}, \tag{12}$$

where $\bar{p}_{tot}^{inl}$ is the area-averaged total pressure at the inlet.

Table 2
Grid resolution (δx), total number of cells (N_c, N_m, N_f), deviation of $|\bar{u}|$ to the next coarser grid, and y^+ for each grid.

Grid	δx	Nr. of cells	Deviation [%]	y^+
Coarse	$d/50$	$N_c = 5 \cdot 10^6$	–	<7
Medium	$d/100$	$N_m = 40 \cdot 10^6$	0.7	<3
Fine	$d/200$	$N_f = 300 \cdot 10^6$	0.1	<1

3. Results

This section presents the results addressing the research questions posed in Section 1. First, a grid refinement study is conducted in Section 3.1 to answer question 1. Next, Section 3.2 compares simulation results for Newtonian fluids under different inflow conditions with MRV measurements, addressing questions 2 and 3. Finally, Section 3.3 examines the differences between Newtonian and non-Newtonian flow characteristics, addressing question 4.

The flow simulations were conducted on the central processing unit (CPU) partition of the Jülich Research on Exascale Cluster Architectures (JURECA-DC) supercomputer [41] of the Jülich Supercomputing Centre (JSC), Forschungszentrum Jülich, Germany. Each node contains two AMD EPYC 7742 processors with 64 cores each and 2.25 GHz, and 512 GB DDR4 memory.

3.1. Grid refinement study

To guarantee a sufficiently high grid resolution, the velocity magnitude averaged over the red centerline illustrated in Fig. 3(a) $|\bar{u}|$ is first analyzed. For a better orientation, the characteristic points $P_1 - P_4$ are also shown in the figure, where P_2 is the point with the highest local quantity $|u|$ along the centerline. Note that $|u|$ is not averaged over the complete centerline, because after P_3 the computational domain starts to deviate slightly from the 3D model used for measurements. The outlets of the MRV measurements are widened to assure a smooth connection to the MRV devices, which also deforms the bulge slightly, cf. Section 2.2. Therefore, $|\bar{u}|$ is computed for all points between the inlet and P_3.

Computational grids with three resolutions are investigated, i.e., a coarse grid with $\delta x = d/50$ and a total number of $N_c = 5 \cdot 10^6$ cells, a medium grid with $\delta x = d/100$ and $N_m = 40 \cdot 10^6$ cells, and a fine grid with $\delta x = d/200$ and $N_f = 300 \cdot 10^6$ cells. The results for $|\bar{u}|$ are summarized in Table 2, where the deviation of $|\bar{u}|$ to the next coarser grid is provided in the last column. Whereas the deviation of $|\bar{u}|$ between the medium and coarse grid is $\frac{|\bar{u}|_{medium} - |\bar{u}|_{coarse}}{|\bar{u}|_{medium}} \cdot 100 = 0.7\%$, it reduces to only $\frac{|\bar{u}|_{fine} - |\bar{u}|_{medium}}{|\bar{u}|_{fine}} \cdot 100 = 0.1\%$ between the fine and medium grid. Since a gain in accuracy of only 0.1% does not justify the increased computational costs from N_m to N_f, the medium grid is the most reasonable choice. In fact, $|\bar{u}|$ of the simulation with the medium grid deviates only by 3.3% from the MRV measurement.

A common indicator for assessing the near-wall resolution is $y^+ = u_\tau \cdot y^* / \mu$, where y^* is the wall distance, and $u_\tau = \sqrt{\sigma^{WSS}/\rho}$ the friction velocity. A y^+ value around 1 is required for resolving the viscous sublayer. The maximum values of the three grids are shown in Table 2, i.e., $y_c^+ < 7$, $y_m^+ < 3$, and $y_f^+ < 1$. It is worth noting that in case of the medium grid in the majority of the flow field $y_m^+ < 1$ is observed. That is, $1 < y_m^+ < 3$ is only reached at very few cells, e.g., near P_2. If one weighs the additional computational costs for further refinement against the relatively small further reduction of the y^+ values, it is justified to use the grid with the medium resolution for the remaining simulations.

The choice for using the medium grid is further underlined by an analysis of the near-wall resolution for $|u|$ in cross-sectional areas at P_2. In Fig. 3(b), which shows these areas for the coarse, medium, and fine grid, it can be seen that the main flow characteristics are captured by all three simulations. However, the profiles of $|u|$ in Fig. 3(c) along

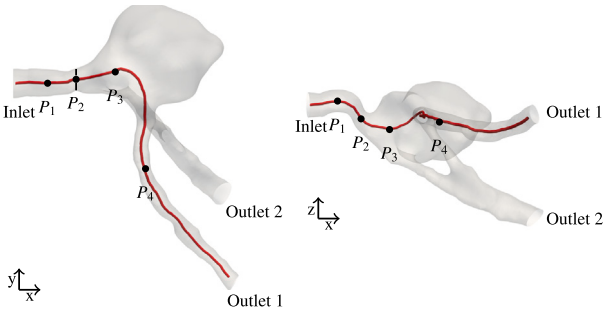

(a) Centerline between the inlet and outlet 1.

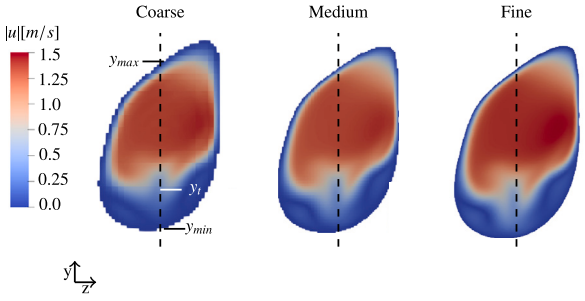

(b) Velocity magnitude $|u|$ for different grid resolutions at the cross-sectional area at P_2 with the normal vector in the x-direction, represented by the black line in Fig. 3a.

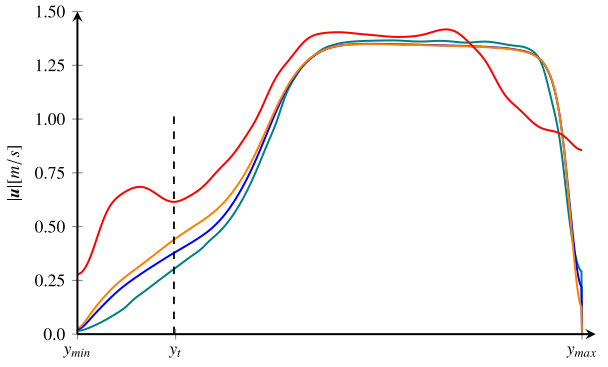

(c) Profiles of the velocity magnitude $|u|$ for the coarse (green), medium (blue), and fine (orange) grids along the dashed lines shown in Fig. 3a compared to the MRV measurements (red).

Fig. 3. Analysis of the grid resolution.

the dashed lines between y_{min} and y_{max} from Fig. 3(b) reveal that the profile based on the simulation with the coarse grid (green) misses the turning point at y_t, which is captured well by the simulations based on the medium (blue) and fine (orange) grids. The profile of the MRV measurements (red) highlights the challenge of the method in general, which has already been mentioned in Section 1, i.e., a good accuracy near the centerline, but difficulties in measuring near-wall velocities.

3.2. Analysis of different inflow conditions for a Newtonian fluid

In this section, the influence of the different inflow conditions that have been introduced in Section 2.2 is analyzed for simulations with a Newtonian fluid. Fig. 4(a) shows $|u|$ at the inflow area. The interpolated inflow condition determines the centerline velocity and interpolates the

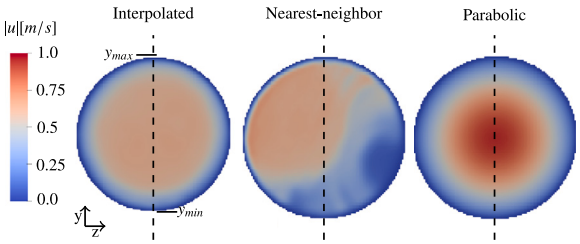

(a) Velocity magnitude $|\boldsymbol{u}|$ for the interpolated inflow condition, inflow condition based on the nearest-neighbor algorithm, and parabolic inflow at the inlet areas with the normal vector in the x-direction.

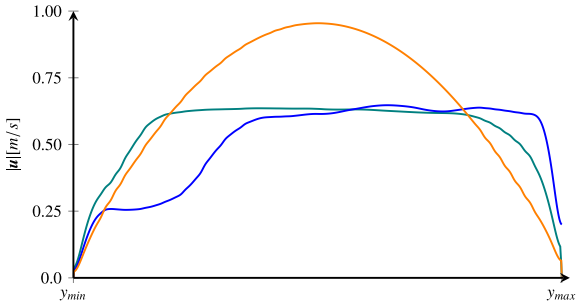

(b) Profiles of the velocity magnitude $|\boldsymbol{u}|$ for the interpolated inflow condition (green), inflow condition based on the nearest-neighbor algorithm (blue), and parabolic inflow area (yellow) along the black dashed lines in Fig. 4a.

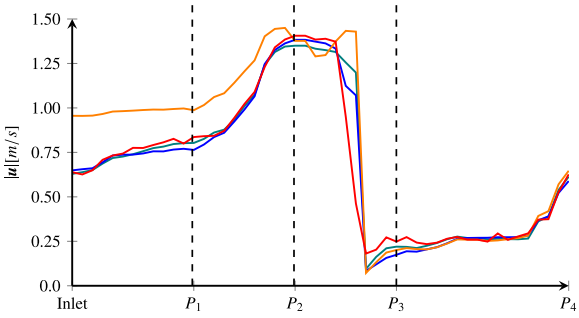

(c) $|\boldsymbol{u}|$ along the centerline for simulations based on the interpolated inflow condition (green), inflow condition based on the nearest-neighbor algorithm (blue), and parabolic inflow area (yellow), compared to the MRV measurements (red).

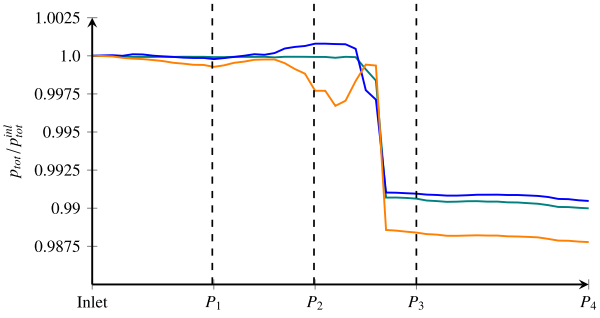

(d) p_{tot}/p_{tot}^{inl} along the centerline for simulations based on the interpolated inflow condition (green), inflow condition based on the nearest-neighbor algorithm (blue), and parabolic inflow area (yellow).

Fig. 4. Analysis of the velocity magnitude $|\boldsymbol{u}|$ and normalized total pressure p_{tot}/p_{tot}^{inl} to evaluate different inflow conditions.

velocities between the centerline and the wall. The nearest-neighbor algorithm yields a similar velocity magnitude near the centerline, but the near-wall velocities deviate from the interpolated inflow condition. Notably, the velocities are unbalanced on either side of the dashed line. The parabolic inflow condition has the highest centerline velocities.

A closer look at the inflow velocity profiles is given in Fig. 4(b). While the profile of the parabolic inflow condition is – as expected – symmetric with an excessive center velocity, and the profile of the interpolated inflow condition is nearly symmetric, the inflow condition based on the nearest-neighbor algorithm shows again no symmetric behavior.

Fig. 4(c) compares the centerline velocity magnitude $|\boldsymbol{u}|$ from simulations using the three inflow conditions with the MRV measurements. In contrast to the grid refinement study, this comparison focuses on the region between the inlet and P_4 (see Fig. 3(a)). Despite the differences between the MRV geometry and simulation domain, the general trend of centerline velocities when exiting the bulge and re-entering the vessel towards Outlet 1 is visible up to P_4.

The simulation using the interpolated inflow condition closely matches the MRV measurements, except for slight underpredictions near P_2. Similarly, the nearest-neighbor inflow condition also shows good agreement, except for minor underpredictions near P_1. In contrast, the simulation results using the parabolic inflow condition results in large deviations from the MRV measurements between the inlet and P_3. However, beyond P_3, the flow appears to recover, as no substantial differences are observed among the three simulations.

A quantitative assessment of the centerline velocities is given with the help of the mean absolute percentage error (MAPE) e_{MAPE}

$$e_{MAPE} = \frac{1}{N}\sum_{i=0}^{N}\left(\frac{\| \boldsymbol{u}|_{\mathrm{LB}}(i) - |\boldsymbol{u}|_{\mathrm{MRV}}(i)|}{|\boldsymbol{u}|_{\mathrm{MRV}}^{max}}\right)\cdot 100, \tag{13}$$

where N stands for the number of centerline points, and the superscript max for the maximum value along the centerline. The simulation results using the interpolated inflow condition have with $e_{MAPE} = 3.12\%$ the lowest error, followed by $e_{MAPE} = 3.18\%$ for the inflow condition based on the nearest-neighbor algorithm, and $e_{MAPE} = 9.85\%$ for the parabolic inflow condition.

The distributions of p_{tot}/p_{tot}^{inl} along the centerline for simulations based on the three inflow conditions are shown in Fig. 4(d), where p_{tot}^{inl} is the total pressure at the center of the inlet area. Note that a comparison to MRV data is not possible, since only velocity fields are measured. The simulations with the inflow condition based on the nearest-neighbor algorithm and the interpolated inflow condition have a similar distribution of the normalized total pressure. In fact, the total pressure of the results based on the nearest-neighbor inflow increases slightly near P_2 due to the larger peak velocities compared to the case with the interpolated inflow condition (See Fig. 4(c)). However, the distribution of the normalized total pressure for the simulation with the parabolic inflow condition is characterized by a local minimum near P_2, and a much lower total pressure after P_3, compared to the other two cases.

The question remains whether or not the previously mentioned deviations affect the bulge of the aneurysm. Therefore, its influence on the distribution of the WSS and the WNS in the vicinity of the bulge is analyzed. Fig. 5(a) presents the WSS magnitude on the blood vessel surface for the three simulations. To aid orientation, surface locations S_1-S_5 (marked in Fig. 5(a)) correspond to characteristic regions of WSS, similar to points P_1-P_4 in Fig. 3(a). S_5 is located at the junction where the vessel branches towards Outlets 1 and 2.

In all three cases, the highest WSS occurs near S_2, which is expected since the vessel narrows at this location, leading to increased velocity and a strong velocity gradient near the wall. The interpolated inflow simulation predicts high WSS values near S_3, S_4, and S_5, whereas the nearest-neighbor approach results in lower WSS in these regions, particularly near S_3. The parabolic inflow condition produces WSS distributions similar to those of the interpolated inflow condition.

Fig. 5(b) shows the WNS distribution mapped onto the vessel surface for all three simulations. The highest WNS values are observed near S_1 in all cases. Near S_1, the parabolic inflow condition yields similar WNS values to the interpolated inflow condition, whereas the nearest-neighbor method underpredicts the WNS.

Additionally, local differences exist between the three cases. For example, at the vascular bifurcation (highlighted by a dashed circle),

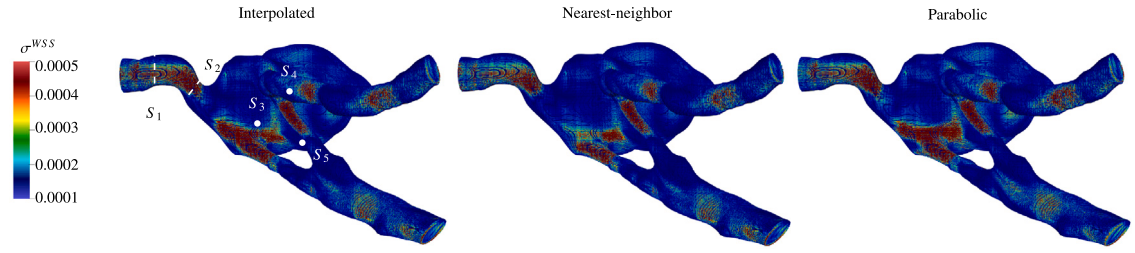

(a) WSS for the simulations with an interpolated inflow condition, inflow based on the nearest-neighbor algorithm, and a parabolic inflow.

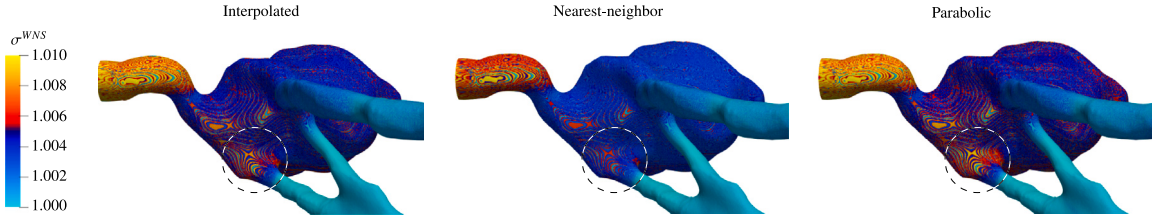

(b) WNS for the simulations with an interpolated inflow condition, inflow based on the nearest-neighbor algorithm, and a parabolic inflow.

Fig. 5. Analysis of the WSS and WNS to evaluate different inflow conditions.

Table 3
Minimum and maximum of the WSS components in $[Pa]$ in the x-, y-, and z-directions, as well as the magnitude of the WSS, and the maximum of the WNS for the simulations with the interpolated inflow condition, the inflow condition based on the nearest-neighbor algorithm, and the parabolic inflow condition.

Inflow condition	$\sigma^{WSS}_{x,min}$	$\sigma^{WSS}_{x,max}$	$\sigma^{WSS}_{y,min}$	$\sigma^{WSS}_{y,max}$	$\sigma^{WSS}_{z,min}$	$\sigma^{WSS}_{z,max}$	$\lvert\sigma^{WSS}_{min}\rvert$	σ^{WSS}_{max}	σ^{WNS}_{max}
Interpolated	−0.0051	0.0045	−0.0029	0.0041	−0.0044	0.0054	0.0073	0.0082	1.017
Nearest-neighbor	−0.0043	0.0043	−0.0031	0.0035	−0.0036	0.0039	0.0064	0.0067	1.037
Parabolic	−0.0039	0.0038	−0.0038	0.0041	−0.0047	0.0057	0.0072	0.0081	1.016

Table 4
Minimum and maximum of the WSS components in $[Pa]$ in the x-, y-, and z-directions, as well as the magnitude of the WSS, and the maximum of the WNS for the simulations with Newtonian fluid flow and non-Newtonian flow behavior.

Fluid behavior	$\sigma^{WSS}_{x,min}$	$\sigma^{WSS}_{x,max}$	$\sigma^{WSS}_{y,min}$	$\sigma^{WSS}_{y,max}$	$\sigma^{WSS}_{z,min}$	$\sigma^{WSS}_{z,max}$	$\lvert\sigma^{WSS}_{min}\rvert$	σ^{WSS}_{max}	σ^{WNS}_{max}
Newtonian	−0.0051	0.0045	−0.0029	0.0041	−0.0044	0.0054	0.0073	0.0082	1.017
non-Newtonian (CY model)	−0.0212	0.0289	−0.0178	0.0187	−0.0270	0.0347	0.0387	0.0489	1.020

a high WNS is expected due to the small curvature radius. Accurate computation of fluid mechanical quantities in such regions is crucial for reliable rupture risk assessment. However, in this area, the nearest-neighbor approach underestimates WNS compared to the interpolated inflow method, while the parabolic inflow condition results in an overprediction.

Table 3 emphasizes the tendency of an underpredicted WSS for the simulation based on the nearest-neighbor algorithm, compared to the case with the interpolated inflow condition. For the WSS components in the x-, y-, and z-directions, whose orientations are shown in Fig. 3(a), the simulations based on the nearest-neighbor algorithm have a much smaller range between the minimum and maximum values, compared to the interpolated inflow condition. This is confirmed by the minimum and maximum WSS magnitudes in the table, e.g., σ^{WSS}_{max} for the nearest-neighbor inflow is 18.3% lower than for the interpolated inflow. However, although the parabolic inflow shows differences to the interpolated case for some WSS components, the minimum and maximum values of the WSS magnitude have only minor deviations.

The maximum WNS for the interpolated and parabolic inflow conditions is nearly the same. However, in contrary to the underpredicted WNS of the case with the nearest-neighbor algorithm at S_1, σ^{max} appears to be larger than the other two cases.

In summary, the simulation results using the interpolated inflow condition show the best agreement with MRV centerline velocity measurements and provide a reasonable distribution of WSS and WNS. The parabolic inflow condition tends to overpredict the centerline velocity between the inflow region and P_3 while underpredicting normalized total pressure near P_2 and beyond P_3. The nearest-neighbor inflow condition underpredicts WSS and exhibits inconsistencies in WNS, making it unsuitable for rupture risk analysis. Therefore, the interpolated inflow condition is selected for the next section, which examines non-Newtonian blood flow behavior.

3.3. Comparison of Newtonian and non-Newtonian fluids

Results for simulations with the non-Newtonian CY model are shown in Fig. 6. The WSS based on the CY model, which is given in Fig. 6(a), is significantly larger than the WSS based on the Newtonian flow in Fig. 5(a). These differences are especially visible in the region of the geometric transition from the narrow vessel at S_2 to the bulge near S_3. The WNS, as shown in Fig. 6(b), is lower compared to the WNS in the case of the Newtonian flow in Fig. 5(b) at taperings, e.g., the tapering at P_2, or before bifurcations, e.g, the location inside of the dashed circle. Such differences between Newtonian and non-Newtonian models are crucial for a reliable evaluation of the rupture risk.

Fig. 6(c) depicts the distributions of $|\boldsymbol{u}|$ along the centerline for the simulations with a Newtonian fluid (green) and the CY model for a non-Newtonian (black) fluid. Generally, the centerline velocity computed by the CY model tends to be lower than the centerline velocity of the Newtonian flow. This matches with the observations in [42], who report much larger centerline velocities of Newtonian blood flow in acapillary with 70° inclination, compared to non-Newtonian flow. The same trend is observed for the velocity gradients along the centerline.

Fig. 6(d) depicts the distributions of p_{tot}/p^{inl}_{tot} along the centerline for the simulations with a Newtonian fluid (green) and the CY

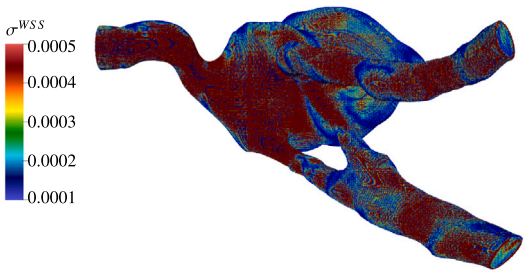

(a) WSS for the simulation with the CY model for non-Newtonian fluid flow.

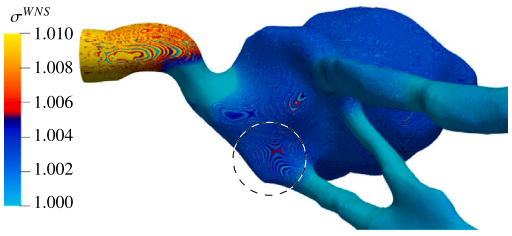

(b) WNS for the simulation with the CY model for non-Newtonian fluid flow.

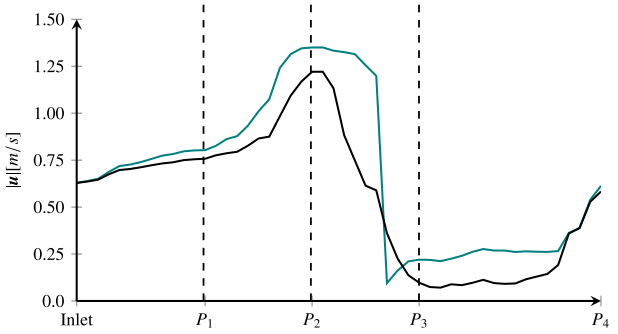

(c) $|u|$ along the centerline for simulations with Newtonian fluid flow (green) and the CY model for non-Newtonian (black) fluid flow.

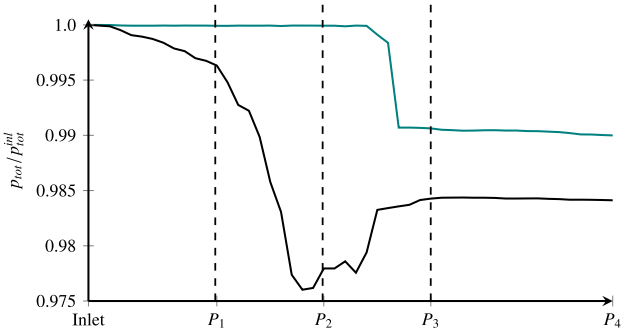

(d) p_{tot}/p_{tot}^{inl} along the centerline for simulations with Newtonian fluid flow (green) and the CY model for non-Newtonian (black) fluid flow.

Fig. 6. Analysis of the WSS, WNS, velocity magnitude $|u|$ and normalized total pressure p_{tot}/p_{tot}^{inl} to evaluate Newtonian and non-Newtonian flow behavior.

model for a non-Newtonian (black) fluid. p_{tot}/p_{tot}^{inl} of the case with the non-Newtonian fluid is generally lower than for the case with the Newtonian fluid, which comes from the generally lower velocities shown in Fig. 6(c) and causes a reduction of the dynamic pressure.

Table 4 reveals that the CY model yields a 6–7-fold greater WSS than the Newtonian model, which matches with the observations in [21], where differences in the WSS distribution between Newtonian and non-Newtonian blood models in an artery tree are investigated. Table 4 also shows, that the maximum WNS value of the CY model is only slightly higher compared to the Newtonian case.

4. Summary and discussion

In this study, MRV measurements were coupled with CFD simulations to develop a new method for analyzing cerebral aneurysms, leveraging the strengths of both approaches. The 5-fold scaled geometry allows for accurate, patient-specific inflow conditions, while the simulation provides highly resolved flow data across the entire domain. This enables better near-wall velocity and WSS estimation, which would be less accurate even with the scaled measurements, and allows for the computation of quantities that cannot be measured directly, such as the 3D pressure field. The method mitigates the individual weaknesses of each approach: the low resolution of MRV measurements and the risk of incorrect flow topologies in simulations due to inaccurate inflow conditions.

The proposed method was tested using a reconstructed geometry from a patient with a cerebral aneurysm. Three inflow conditions were evaluated:

1. **Interpolated inflow**
   MRV data were interpolated onto the simulation grid, with zero-velocity points added at walls to enforce the no-slip condition if measurements points exceed the simulation domain.
2. **Nearest-neighbor inflow**
   Each grid cell was assigned the velocity of the nearest MRV measurement point.
3. **Parabolic inflow**
   A parabolic velocity profile was prescribed at the inlet.

A grid refinement study was first conducted using the interpolated inflow condition to determine the resolution needed to accurately capture both near-wall and centerline velocities. Next, simulation results using all three inflow conditions were compared to MRV measurements. The interpolated inflow condition provided the best agreement with centerline velocity magnitudes. The nearest-neighbor inflow condition resulted in underpredictions of WSS and inconsistencies in WNS. The parabolic inflow condition led to overpredictions in centerline velocity and underpredictions in total pressure distribution. Additionally, it has been illustrated how the MRV measurements fail to realistically capture near-wall velocities for computing the WSS.

Based on these findings, the interpolated inflow condition was used to compare Newtonian and non-Newtonian flow models. The non-Newtonian model exhibited lower centerline velocities and total pressure compared to the Newtonian case, consistent with observations in [42]. Additionally, the CY model predicted higher WSS, particularly near the transition from the narrow vessel to the aneurysmal bulge. The WNS of the non-Newtonian model was also lower at vessel taperings and before bifurcations compared to the Newtonian case.

The grid refinement study (Section 3.1) addressed question 1 from Section 1, determining the required grid resolution for accurate simulations. To maintain simplicity in implementing the interpolated and nearest-neighbor inflow conditions, uniformly refined grids were used, similar to those in [43], which inspired this study. Future work could explore locally refined grids to further improve accuracy while ensuring $y^+ < 1$ across the entire domain without excessive grid cell increases.

Additionally, the simulations assumed rigid walls with static grids, whereas in vivo conditions involve vessel wall compliance [44]. Currently, the LB method in the m-AIA framework does not support fluid–structure interaction. Even if vessel wall compliance were integrated, the mechanical properties of the wall, which are not yet measurable, would need to be determined. Advances in MRV resolution may eventually allow estimation of these properties from wall motion, as suggested in [45].

The results in Section 3.2 demonstrated that simulations using the interpolated inflow condition accurately reproduced centerline velocities from MRV measurements, addressing question 2 from Section 1. Additionally, they outperformed the other inflow conditions, answering question 3. While the nearest-neighbor and parabolic inflow conditions require less effort to implement, the accuracy gain from interpolation justifies the additional complexity.

In this study, steady flow conditions allowed all inflow profiles to be precomputed before simulation. However, patient-specific flow replication requires unsteady, pulsatile flow conditions. Future work could test the method with time-resolved MRV measurements [46], where inflow conditions would need periodic updates. Under these conditions, the interpolated profile would likely become less symmetric, while the parabolic profile would remain computationally simpler since it can be scaled with a pulsatile function.

The results in Section 3.3 highlighted the importance of using non-Newtonian models for accurately determining WSS, addressing question 4 from Section 1. In particular, the CY model predicted higher WSS near the transition from the narrow vessel to the bulge, which is critical for rupture risk assessment and aligns with findings from [21]. Blood, like the non-Newtonian model fluid, behaves as a shear-thinning fluid. On the centerline the shear rate is particularly low due to velocity gradients near zero, therefore the viscosity is increased compared to a Newtonian fluid. Near the walls the gradients are high, so that the shear rate is high and the viscosity is low. This results in a tendency of the flow increasing the velocities toward the wall and also the gradient and the WSS and consequently reducing the velocity on the centerline, with respect to a Newtonian profiles.

Since the method has been tested on only a single geometry, further validation using additional patient data is needed to generalize the findings. Nonetheless, integrating MRV-based inflow conditions with non-Newtonian LB simulations has demonstrated strong potential as a foundation for personalized cerebral aneurysm assessments, including rupture risk evaluation and implant design, such as flow diverters or stents.

5. Conclusion

In this study, a method combining MRV measurements and CFD simulations was developed to leverage patient-specific inflow data and provide high-resolution flow analysis for cerebral aneurysms. The interpolated inflow condition demonstrated superior accuracy in reproducing MRV measurements compared to parabolic and nearest-neighbor approaches, which is more important than the lower implementation effort of the other two inflow conditions. Additionally, the incorporation of non-Newtonian models, particularly the CY model, proved essential for accurately capturing WSS distributions, especially in critical regions such as vessel taperings and aneurysm bulges. These findings highlight the potential of this method to improve patient-specific diagnostics, assess rupture risk, and guide the design of medical devices such as stents or flow diverters.

To further advance this approach, future studies should validate the method with a larger dataset of patient geometries and investigate its performance under unsteady, pulsatile flow conditions using time-resolved MRV measurements. Incorporating locally refined grids near vessel walls could enhance accuracy while maintaining computational efficiency. Expanding the method to include fluid–structure interactions by coupling LB simulations with structural solvers could also offer a more realistic representation of vessel wall compliance, particularly as advancements in MRV resolution enable better estimation of wall properties. These developments would pave the way for a more robust and personalized evaluation of aneurysm rupture risk and treatment planning.

CRediT authorship contribution statement

Mario Rüttgers: Writing – original draft, Visualization, Methodology, Investigation, Conceptualization. **Moritz Waldmann:** Writing – review & editing, Software, Methodology, Conceptualization. **Shota Ito:** Writing – review & editing, Software, Methodology. **Carolin Wüstenhagen:** Writing – review & editing, Methodology, Data curation. **Sven Grundmann:** Writing – review & editing, Supervision, Conceptualization. **Martin Brede:** Writing – review & editing, Supervision, Conceptualization. **Andreas Lintermann:** Writing – review & editing, Supervision, Project administration, Funding acquisition, Conceptualization.

Ethics statement

This study utilized anonymized patient imaging data. Informed consent was obtained from all participants.

Declaration of competing interest

The authors declare that they have no known competing financial interests or personal relationships that could have appeared to influence the work reported in this paper.

Acknowledgments

The research leading to these results has been conducted in the HANAMI project, which receives funding from the European Union Horizon Europe Programme - Grant Agreement Number 101136269 under the call HORIZON-EUROHPC-JU-2022-INCO-04. The authors gratefully acknowledge the computing time granted on the supercomputer JURECA-DC [41] at Forschungszentrum Jülich.

References

[1] D.M. Sforza, C.M. Putman, J.R. Cebral, Hemodynamics of cerebral aneurysms, Annu. Rev. Fluid Mech. 41 (1) (2009) 91–107.
[2] J.R. Cebral, M.A. Castro, J.E. Burgess, R.S. Pergolizzi, M.J. Sheridan, C.M. Putman, Characterization of cerebral aneurysms for assessing risk of rupture by using patient-specific computational hemodynamics models, Am. J. Neuroradiol. 26 (10) (2005) 2550–2559.
[3] T.-M. Liou, C.-C. Liao, Flowfields in lateral aneurysm models arising from parent vessels with different curvatures using PTV, Exp. Fluids 23 (4) (1997) 288–298.
[4] Y. Hoi, S. Woodward, M. Kim, D. Taulbee, H. Meng, Validation of CFD simulations of cerebral aneurysms with implication of geometric variations, J. Biomech. Eng. 128 (2007) 844–851.
[5] C. Roloff, D. Stucht, O. Beuing, P. Berg, Comparison of intracranial aneurysm flow quantification techniques: standard PIV vs stereoscopic PIV vs tomographic PIV vs phase-contrast MRI vs CFD, J. NeuroInterventional Surg. 11 (3) (2019) 275–282.
[6] S.V. Frolov, S.V. Sindeev, J.S. Kirschke, P. Arnold, S. Prothmann, D. Liepsch, A. Balasso, A. Potlov, I. Larrabide, S. Kaczmarz, CFD and MRI studies of hemodynamic changes after flow diverter implantation in a patient-specific model of the cerebral artery, Exp. Fluids 59 (11) (2018) 176.
[7] D. Liepsch, S. Sindeev, S. Frolov, An impact of non-Newtonian blood viscosity on hemodynamics in a patient-specific model of a cerebral aneurysm, J. Phys.: Conf. Ser. 1084 (2018) 012001.
[8] J.L. Berry, A. Santamarina, J.E. Moore Jr., S. Roychowdhury, W.D. Routh, Experimental and computational flow evaluation of coronary stents, Ann. Biomed. Eng. 28 (4) (2000) 386–398.
[9] S. Moravec, D. Liepsch, Flow investigations in a model of a three-dimensional human artery with Newtonian and non-Newtonian fluidS. Part I, Biorheology 20 (6) (1983) 745–759.
[10] A. Balasso, J.S. Bauer, T. Liebig, F. Dorn, C. Zimmer, D. Liepsch, S. Prothmann, Evaluation of intra-aneurysmal hemodynamics after flow diverter placement in a patient-specific aneurysm model, Biorheology 51 (6) (2015) 341–354.
[11] S.V. Frolov, S.V. Sindeev, D. Liepsch, A. Balasso, Experimental and CFD flow studies in an intracranial aneurysm model with Newtonian and non-Newtonian fluids, Technol. Health Care 24 (2016) 317–333.
[12] D. Liepsch, An introduction to biofluid mechanics—basic models and applications, J. Biomech. 35 (4) (2002) 415–435.
[13] T.T. Nguyen and, Y. Biadillah, R. Mongrain, J. Brunette, J.-C. Tardif, O.F. Bertrand, A method for matching the refractive index and kinematic viscosity of a blood analog for flow visualization in hydraulic cardiovascular models, J. Biomech. Eng. 126 (4) (2004) 529–535.

[14] G. Mulder, A.C.B. Bogaerds, P. Rongen, F.N. van de Vosse, On automated analysis of flow patterns in cerebral aneurysms based on vortex identification, J. Engrg. Math. 64 (4) (2009) 391–401.
[15] K. Fukazawa, F. Ishida, Y. Umeda, Y. Miura, S. Shimosaka, S. Matsushima, W. Taki, H. Suzuki, Using computational fluid dynamics analysis to characterize local hemodynamic features of middle cerebral artery aneurysm rupture points, World Neurosurg. 83 (1) (2015) 80–86.
[16] T. Passerini, L.M. Sangalli, S. Vantini, M. Piccinelli, S. Bacigaluppi, L. Antiga, E. Boccardi, P. Secchi, A. Veneziani, An integrated statistical investigation of internal carotid arteries of patients affected by cerebral aneurysms, Cardiovasc. Eng. Technol. 3 (1) (2012) 26–40.
[17] S. Voß, O. Beuing, G. Janiga, P. Berg, Multiple aneurysms anatomy challenge 2018 (MATCH)—Phase Ib: Effect of morphology on hemodynamics, PLOS ONE 14 (5) (2019) e0216813.
[18] K. Takizawa, K. Schjodt, A. Puntel, N. Kostov, T.E. Tezduyar, Patient-specific computational fluid mechanics of cerebral arteries with aneurysm and stent, in: Multiscale Simulations and Mechanics of Biological Materials, John Wiley & Sons Ltd, Oxford, UK, 2013, pp. 119–147.
[19] S. Voß, O. Beuing, G. Janiga, P. Berg, Stent-induced vessel deformation after intracranial aneurysm treatment – A hemodynamic pilot study, Comput. Biol. Med. 111 (2019) 103338.
[20] B. Liu, D. Tang, Influence of non-Newtonian properties of blood on the wall shear stress in human atherosclerotic right coronary arteries, Mol. Cell. Biomech. : MCB 8 (2011) 73–90.
[21] J.C. Weddell, J. Kwack, P.I. Imoukhuede, A. Masud, Hemodynamic analysis in an idealized artery tree: Differences in wall shear stress between Newtonian and non-Newtonian blood models, PLOS ONE 10 (2015) 1–23.
[22] H. Yi, Z. Yang, M. Johnson, L. Bramlage, B. Ludwig, Hemodynamic characteristics in a cerebral aneurysm model using non-Newtonian blood analogues, Phys. Fluids 34 (10) (2022) 103101.
[23] H. Vaseghnia, E. Jettestuen, K.E. Teigen Giljarhus, A. Hiorth, Evaluation of WSS distributions in pulsatile non-Newtonian fluid flows using the MRT-LB model, in: A.C. Benim, R. Bennacer, A.A. Mohamad, P. Ocłoń, S.-H. Suh, J. Taler (Eds.), Advances in Computational Heat and Mass Transfer, Springer Nature Switzerland, Cham, 2024, pp. 114–123.
[24] H. Vaseghnia, E. Jettestuen, K.E. Teigen Giljarhus, J.L. Vinningland, A. Hiorth, Effects of hematocrit and non-Newtonian blood rheology on pulsatile wall shear stress distributions in vascular anomalies: A multiple relaxation time lattice Boltzmann approach, Phys. Fluids 36 (8) (2024) 083102.
[25] C. Stokes, D. Ahmed, N. Lind, F. Haupt, D. Becker, J. Hamilton, V. Muthurangu, H. Von Tengg-Kobligk, G. Papadakis, S. Balabani, V. Díaz-Zuccarini, Aneurysmal growth in type-B aortic dissection: assessing the impact of patient-specific inlet conditions on key haemodynamic indices, J. R. Soc. Interface 20 (2023).
[26] S. Black, C. Maclean, P. Hall Barrientos, K. Ritos, A. McQueen, A. Kazakidi, Calibration of patient-specific boundary conditions for coupled CFD models of the aorta derived from 4D Flow-MRI, Front. Bioeng. Biotechnol. 11 (2023).
[27] P. Fillingham, S. Rane Levendovszky, J. Andre, M. Bindschadler, S. Friedman, M. Kurt, A. Aliseda, M.R. Levitt, Noninvasive, patient-specific computational fluid dynamics simulations of dural venous sinus pressures in idiopathic intracranial hypertension, Brain Multiphysics 5 (2023) 100081.
[28] C.J. Elkins, M. Markl, N. Pelc, J. Eaton, 4D Magnetic resonance velocimetry for mean velocity measurements in complex turbulent flows, Exp. Fluids 34 (2003) 494–503.
[29] A. Lintermann, S. Schlimpert, J.H. Grimmen, C. Günther, M. Meinke, W. Schröder, Massively parallel grid generation on HPC systems, Comput. Methods Appl. Mech. Engrg. 277 (2014) 131–153.
[30] A. Lintermann, M. Meinke, W. Schröder, Zonal Flow Solver (ZFS): a highly efficient multi-physics simulation framework, Int. J. Comput. Fluid Dyn. 34 (7–8) (2020) 458–485.
[31] D. Hartmann, M. Meinke, W. Schröder, An adaptive multilevel multigrid formulation for Cartesian hierarchical grid methods, Comput. & Fluids 37 (9) (2008) 1103–1125.
[32] H. Sagan, Hilbert's space-filling curve, in: Space-Filling Curves, Springer New York, New York, NY, 1994, pp. 9–30.
[33] J. Li, W.-K. Liao, A. Choudhary, R. Ross, R. Thakur, W. Gropp, R. Latham, A. Siegel, B. Gallagher, M. Zingale, Parallel netCDF: A high-performance scientific I/O interface, in: SC '03: Proceedings of the 2003 ACM/IEEE Conference on Supercomputing, 2003, pp. 39–39.
[34] X. He, L.S. Luo, Theory of the lattice Boltzmann method: From the Boltzmann equation to the lattice Boltzmann equation, Phys. Rev. E 56 (6) (1997) 6811–6817.
[35] Y.-H. Qian, D. D'Humières, P. Lallemand, Lattice BGK models for Navier-Stokes equation, Europhys. Lett. 17 (6) (1992) 479–484.
[36] M. Bouzidi, M. Firdaouss, P. Lallemand, Momentum transfer of a Boltzmann-lattice fluid with boundaries, Phys. Fluids 13 (11) (2001) 3452–3459.
[37] P. Neofytou, S. Tsangaris, Flow effects of blood constitutive equations in 3D models of vascular anomalies, Internat. J. Numer. Methods Fluids 51 (5) (2006) 489–510.
[38] H. Nguyen, D. Nguyen Ngoc, Incompressible non-Newtonian fluid flows, 2012.
[39] P.J. Carreau, Rheological equations from molecular network theories, Trans. Soc. Rheol. 16 (1) (1972) 99–127.
[40] S. Shibeshi, W. Collins, The rheology of blood flow in a branched arterial system, Appl. Rheol. 15 (2019) 398–405.
[41] D. Krause, P. Thörnig, JURECA: Modular supercomputer at Jülich Supercomputing Centre, J. Large-Scale Res. Facil. 4 (2018) A132.
[42] S. Gore, B. Mazumdar, A. Bit, Effects of inclination of micro-capillary on blood-viscosity of diseased blood in presence of metallic ball, BioNanoScience 8 (2018).
[43] H.E. Morrison, A. Lintermann, S. Grundmann, Hybrid datasets: Incorporating experimental data into Lattice-Boltzmann simulations, Eng. Rep. 2 (6) (2020) e12177.
[44] C. Zhang, M.-C. Villa-Uriol, M. De Craene, J. Pozo, A. Frangi, Time-resolved 3D rotational angiography reconstruction: towardscerebral aneurysm pulsatile analysis, Int. J. Comput. Assist. Radiol. Surg. 3 (2008).
[45] Z. Ma, Y. Zhuang, X. Long, B. Yu, J. Li, Y. Yang, Y. Yu, Modeling and evaluation of biomechanics and hemodynamic based on patient-specific small intracranial aneurysm using fluid-structure interaction, Comput. Methods Programs Biomed. 244 (2024) 107963.
[46] M. Markl, A. Harloff, T. Bley, M. Zaitsev, B. Jung, E. Weigang, M. Langer, J. Hennig, A. Frydrychowicz, Time-resolved 3D MR velocity mapping at 3T: Improved navigator-gated assessment of vascular anatomy and blood flow, J. Magn. Reson. Imaging : JMRI 25 (2007) 824–831.